Anodic oxidation of epitaxial superconductor-semiconductor hybrids

Asbjørn C. C. Drachmann,[1,*] Rosa E. Diaz,[2] Candice Thomas,[2,3] Henri J. Suominen,[1] Alexander M. Whiticar,[1] Antonio Fornieri,[1] Sergei Gronin,[2,3,4] Tiantian Wang,[2,3] Geoffrey C. Gardner,[2,3,4,5] Alex R. Hamilton,[1,6,7] Fabrizio Nichele,[1,8] Michael J. Manfra,[2,3,4,5,9] and Charles M. Marcus[1,†]

[1]Center for Quantum Devices and Microsoft Quantum Lab Copenhagen, Niels Bohr Institute, University of Copenhagen, Universitetsparken 5, 2100 Copenhagen, Denmark
[2]Birck Nanotechnology Center, Purdue University, West Lafayette, Indiana 47907, USA
[3]Department of Physics and Astronomy and Station Q Purdue, Purdue University, West Lafayette, Indiana 47907, USA
[4]Microsoft Quantum Purdue, Purdue University, West Lafayette, Indiana 47907, USA
[5]School of Materials Engineering, Purdue University, West Lafayette, Indiana 47907, USA
[6]School of Physics, University of New South Wales, Sydney, New South Wales 2052, Australia
[7]Australian Research Centre of Excellence in Future Low Energy Electronics Technologies, University of New South Wales, Sydney, New South Wales 2052, Australia
[8]IBM ResearchZurich, Sumerstrasse 4, 8803 Rschlikon, Switzerland
[9]School of Electrical and Computer Engineering, Purdue University, West Lafayette, Indiana 47907, USA

(Received 17 September 2020; revised 28 November 2020; accepted 7 December 2020; published 25 January 2021)

We demonstrate a new fabrication process for hybrid semiconductor-superconductor heterostructures based on anodic oxidation (AO), allowing controlled thinning of epitaxial Al films. Structural and transport studies of oxidized epitaxial Al films grown on insulating GaAs substrates reveal spatial nonuniformity and enhanced critical temperature and magnetic fields. Oxidation of epitaxial Al on hybrid InAs heterostructures with a conducting quantum well show similarly enhanced superconducting properties transferred to the two-dimensional electron gas (2DEG) by proximity effect, with critical perpendicular magnetic fields up to 3.5 T. An insulating AlOx film that passivates the heterostructure from exposure to air is obtained by complete oxidation of the Al. It simultaneously removes the need to strip Al which damages the underlying semiconductor. AO passivation yielded 2DEG mobilities two times higher than similar devices with Al removed by wet etching. An AO-passivated Hall bar showed quantum Hall features emerging at a transverse field of 2.5 T, below the critical transverse field of thinned films, eventually allowing transparent coupling of quantum Hall effect and superconductivity. AO thinning and passivation are compatible with standard lithographic techniques, giving lateral resolution below <50 nm. We demonstrate local patterning of AO by realizing a semiconductor-based Josephson junction operating up to 0.3 T perpendicular.

DOI: 10.1103/PhysRevMaterials.5.013805

I. INTRODUCTION

The recent emergence of epitaxial semiconductor-superconducting hybrid materials has provided numerous experimental systems with highly controllable electronic and superconducting properties [1–14]. Interest has been sparked by theoretical predictions of topological phases in one-dimensional (1D) superconductor-semiconductor hybrids [15,16] with possible application toward topological quantum computing [17]. Alternatively, topological phases can be achieved in 2D systems combining superconductivity with top-down fabricated narrow wires [18–20], Josephson junctions [21–23] or quantum Hall edges in fully 2D systems proximitized by superconductivity [24,25].

In each of these instances, the subgap density of states is a key property of the hybrid system [26,27]. Low subgap density of states, typically extracted from the subgap conductance in a tunneling measurement, is associated with high transparency of the semiconductor-superconductor interface, that is, high Andreev reflection probability [28,29]. Near-unity interface transmission probabilities have been achieved by *in situ* molecular beam growth of epitaxial Al-InAs hybrid heterostructures in different geometries: Vapor-liquid-solid nanowires [1,2], selective area grown nanowires [9,10], and shallow two-dimensional electron gases (2DEGs) [5,6,30]. Recently, similar high-interface transparencies were reported for other hybrid nanowires such as Sn-InSb [12], Ta-InAs [13], and Pb-InAs [14].

Despite their high Andreev reflection probability and resulting hard induced gap, InAs-Al hybrid platforms face two important challenges: (i) surface scattering and reduced mobility resulting from the quantum well being close to the surface, and (ii) limited critical magnetic fields due to the use of Al. Regarding surface scattering, by design the semiconductor wave function must extend to the surface when Al is present. Once the Al is removed, carriers are susceptible

*asbjorn.drachmann@nbi.ku.dk
†chmarcus@microsoft.com

 ©2021 American Physical Society

to surface scattering, resulting in a drop in mobility [31]. Sensitivity to surface chemistry of shallow 2DEGs for similar materials was recently investigated in Ref. [32]. For hybrid heterostructures with Al, a significant contribution to surface scattering is added by the standard Al etching process [5]. Regarding low critical magnetic field, we note that magnetic fields are used in these materials for a variety of purposes, particularly to drive the topological transition [15,16,24,25]. The applied superconductor should have critical fields higher that the field needed to drive the transition. In typical applications of 1D hybrids, a magnetic field, $B_{\|}$, along the axis of the 1D nanowire lowers states by Zeeman splitting into the superconducting gap, where, in the presence of spin-orbit coupling, a topological superconducting phase can appear. An intriguing application of 2D hybrids is to drive the system into the quantum Hall regime by applying a perpendicular magnetic field, $B_{\perp}$, creating edge states that coexist with superconductivity.

High critical fields are found in type-II superconductors such as MoRe, with $B_{c2} \sim 8$ T [4], and NbN with $B_{c2} \sim 25$ T [7]. These materials allow penetration of flux, creating vortices, that decrease Andreev reflection probability when used for proximity effect [7], potentially leading to unwanted subgap state. MoRe and NbN have been deposited *ex situ* on the edge of high mobility quantum-well heterostructures such as GaAs/AlGaAs [3] or Graphene/hBN [4,7], yielding superconducting features within the integer Quantum Hall regime. The studies show moderate Andreev reflection probability, possibly associated with *ex situ* deposition.

To date, superconductors showing high-transparency interfaces with semiconductors, including Al, Sn, Ta, and Pb, have been type I, with relatively low critical magnetic fields, $B_c < 100$ mT in bulk. However, as thin films these same materials show large in-plane critical field, $B_{c,||}$, for instance $B_{c,||} > 8.5$ T reported for a 15-nm-thick layer of Pb [14], and $B_{c,||} > 3$ T for 5- to 7-nm Al films [19]. Though not coupled to a heterostructure, $B_{c,||} > 9$ T was measured [33] on a 2-nm thin Al film and a perpendicular critical field $B_{c,\perp} \sim 3.6$ T was extrapolated [34] from granular aluminum [35,36].

In this work, we develop a method to apply *ex situ* anodic oxidation (AO) to epitaxial Al, the top layer of a heterostructure stack grown by molecular beam epitaxy on III-V substrates. AO is demonstrated to thin the metallic Al, improving its material properties for these applications, and, when AO is applied with higher voltage, to fully oxidize the Al, it results in an insulating AlOx layer and a semiconductor interface that has never been exposed to air. In both applications, local patterning using electron beam lithography is employed.

The rest of the paper is organized as follows: Section II gives experimental details of the AO process. Section III presents structural analysis of anodized Al on insulating GaAs. Section IV presents transport properties of Al on insulating GaAs. Turning to InAs heterostructures with conducting quantum wells, Sec. V presents enhanced superconducting properties after thinning of Al by AO. Passivation of the 2DEG by complete oxidation of Al is presented in Sec. VI, followed by quantum Hall measurements on an AO-passivated Hall bar. Finally, in Sec. VII, a fabrication scheme is presented that provides high-resolution AO patterning.

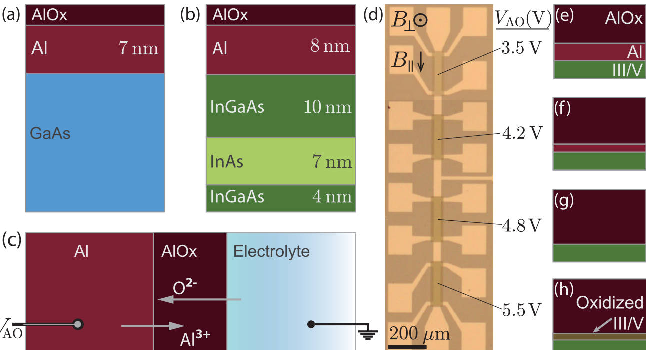

FIG. 1. Hybrid heterostructures grown by molecular beam epitaxy, with Al films on III-V substrates. (a) Sample 1, Al on insulating GaAs (100) substrate. (b) Sample 2, Al capping a shallow InAs heterostructure supporting a two dimensional electron gas. (c) Anodic oxidation with source voltage V_{AO} between the metal (Al) and the electrolyte to drive O^{2-} ions to the Al surface. (d) Optical micrograph of an Al-InAs Hall bar (device α) characterized by four different regions oxidized with different AO voltages, V_{AO}. [(e)–(h)] Regimes of anodic oxidation for V_{AO} between 3.5 V and 5.5 V. [(e)–(g)] Increasing V_{AO} increases oxidation depth, until only alumina is left, as indicated. (h) Further increasing V_{AO} oxidizes the underlying III-V.

II. FABRICATION AND MEASUREMENT

Two heterostructures, denoted samples 1 and 2, were grown by molecular beam epitaxy. Sample 1 consisted of a 7-nm epitaxial Al layer grown on an *insulating* GaAs substrate, see Fig. 1(a). This sample allowed study of the Al film as the only conductor. Sample 2 consists of an 8-nm epitaxial Al layer grown on a shallow InAs heterostructure, see Fig. 1(b). Sample 2 allows the effects of AO on Al coupled to an InAs quantum-well 2DEG to be investigated, including superconducting proximity effect for thin Al, and surface passivation for fully oxidized Al.

The AO technique we employ is widely used in industry [37,38]. Under atmospheric conditions, Al forms a native oxide saturating at ~3 nm [39]. AO enables a deeper oxidation, with a depth controlled by an applied voltage V_{AO}. Figure 1(c) sketches the AO setup: V_{AO} is applied between the Al and an electrolyte solution in which the substrate is submerged. The voltage drives ions to the Al-AlOx surface, increasing the oxidation depth. Depending on the electrolyte used, two oxide morphologies can form [38]. The one of interest is thin and uniform, with V_{AO} controlling the oxidation depth. This oxide type, described in Refs. [38,40], can be achieved by implementing tartaric acid, 3% by mass, as electrolyte, regulated to pH ~ 5.5 by ammonium hydroxide. A voltage-dependent oxide thickness of 1.3 nm/V is expected. Further details of the setup are given in Sec. A of supplemental material (SM) [41]. Standard electron beam lithography was used to pattern elongated Hall bars from an InAs 2DEG heterostructure, shown in Fig. 1(d) and from Al on GaAs, in SM Sec. B [41].

On sample 1 [Fig. 1(a)], AO was patterned into areas with $V_{AO} = 4$ V. Two areas on the sample, designated AO_I and AO_{II}, were exposed simultaneously to check for consistency. A subsequent wet etch defined elongated Hall bars in both anodized and unprocessed epitaxial Al.

On sample 2 [Fig. 1(b)], grown on an InP substrate, a standard III-V wet mesa etch defined Hall bars and bonding pads for ohmic contacts. In four sequential lithography steps, AO was performed at voltages $V_{AO} = 3.5, 4.2, 4.8,$ and 5.5 V on different areas, as shown in Fig. 1(d). Following AO, an 18-nm HfO layer was deposited globally by atomic layer deposition, followed by deposition of patterned Ti-Au gates. Two Hall bars, denoted α and β, each with four AO exposures, were fabricated simultaneously on the same chip, again to check consistency. Figure 1(d) shows Hall bar α. Further InAs fabrication details are given in SM Sec. C [41]. These voltages yielded outcomes of two types: For smaller V_{AO}, the thickness of Al was reduced and its morphology altered, but it remained a metallic conductor. For larger V_{AO}, complete oxidation occurred, as illustrated in Fig. 1(g). Increasing V_{AO} further began to oxidize the semiconductor, leading to increased disorder, as indicated in Fig. 1(h).

Measurements were carried out in various dilution refrigerators, each with a base temperature ~20 mK and a 6-1-1-T vector magnet. Standard ac lock-in techniques were used to apply a small ac current I in the range 1–10 nA while measuring the longitudinal voltage, V_{xx}. Longitudinal resistivity ρ_{xx} was obtained from the measured differential resistance, dV_{xx}/dI, by division with 5.0, the ratio of voltage-probe separation to Hall bar width.

III. ANODIZED Al ON INSULATING GaAs: STRUCTURAL ANALYSIS

To check the uniformity of Al films following AO, sample 1 was characterized with scanning transmission electron microscopy (STEM) and electron energy loss spectroscopy (EELS). STEM sample was prepared (Thermo Fisher dual beam SEM/FIB Helios 4G) with accelerating voltage 500 V for final thinning of the focused ion beam (FIB) lamella. STEM imaging (Thermo Fisher aberration-corrected Themis Z) used an accelerating voltage of 300 kV, giving a resolution of 65 pm. STEM images were acquired along the [110] zone axis in the semiconductor. EELS data acquisition was performed in STEM mode at 300 kV with an energy resolution of 0.75 eV and a dispersion of 0.05 eV.

Figure 2(a) shows a high-angle annular dark-field (HAADF) micrograph of AO_I at the GaAs-Al interface. Three Al hills (dark gray) are distinguishable from GaAs (bright) and AlOx (black). Hills of Al, ~2 nm in height, were observed across the entire cross section. Fast Fourier transform of the hills extracts a crystal growth direction along [110], see SM Sec. D [41]. The origin of the Al hills is not known. Possible explanations include roughness after growth, increased oxidation at grain boundaries or degradation of the lamella during FIB preparation.

EELS was implemented to analyze the elemental configuration [42,43]. Specifically, a study was done to conclude whether the region in between Al hills had metallic Al or only alumina. High resolution STEM micrographs in HAADF mode were acquired at the Al-GaAs interface between Al hills, one is shown in Fig. 2(b). EELS analysis was done at points on a line along the growth direction, see Figs. 2(b) and 2(c). Dual EELS mode was used, allowing simultaneous acquisition of the Al L-edge (~80 eV) and O K-edge

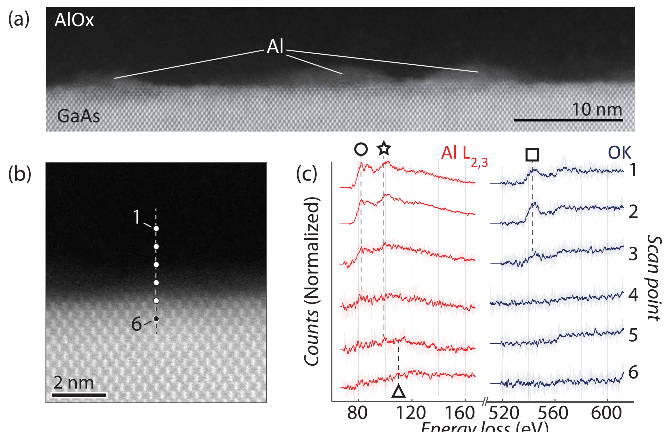

FIG. 2. Transmission electron microscopy study of Al anodized at 4 V on GaAs substrate. (a) Scanning transmission electron micrograph in high-angle annular dark-field (HAADF) mode of AO_I, showing up to 2-nm hills of Al at the GaAs interface. (b) HAADF image of the Al-GaAs interface between Al hills. Electron energy loss spectroscopy (EELS) was performed at 6 different locations (marked by points and separated by 0.3 nm) along the growth direction to gauge material composition. (c) EELS image showing L edge for Al spectra (red) and K edge for O (blue) from scan points 1–6, in (b) with 0.3 nm separation. Symbols indicate composition: (○) AlOx, (⋆) Al or AlOx, (△) GaAs, (□) oxygen.

(~540 eV). All EELS data had a background subtracted, was then normalized and averaged over 20 points.

When GaAs is imaged, a shoulder around 110 eV [marked by △ in Fig. 2(c)] is expected. Metallic aluminum has one peak around 97 eV (⋆) while alumina has two peaks around 79 eV (○) and 98 eV (⋆). Oxygen produces a peak around 540 eV (□). At the Al L-edge, GaAs (△) is evident at points 6 and possibly 5; alumina (○) is evident at points 1 to 3, possibly 4; metallic Al (⋆, no ○) is evident at points 4 and 5. Inspecting the O K-edge, oxygen (□) is only present in points 1–3, indicating that point 4 is metallic Al.

To obtain statistics on the global morphology of the Al after AO, nine additional EELS analyses were conducted in between other Al hills. One region out of 10 failed to show metallic Al, suggesting that roughly 10% of regions between hills are fully oxidized. A collection of broad-view STEM [Fig. 2(a)] were used to extract the fraction of hills to off-hill regions across the film. Hills have an average height of 2 nm and cover roughly one third of the imaged regions. Within the remaining two thirds, ~10% appears fully oxidized. The remaining $2/3 \times 9/10 = 3/5$ contains a thin metallic Al layer. Measurements of the metallic Al thickness between hills span 3 to 6 Å (5 Å on average), corresponding to roughly one to two monolayers (ML) of Al. Additional scans are shown in SM Sec. D [41]. In summary, an uneven, though continuous, Al film is formed by AO.

IV. ANODIZED Al ON INSULATING GaAs: TRANSPORT STUDIES

We investigate the effect of AO on the superconducting properties of the thinned Al films. Critical in-plane magnetic

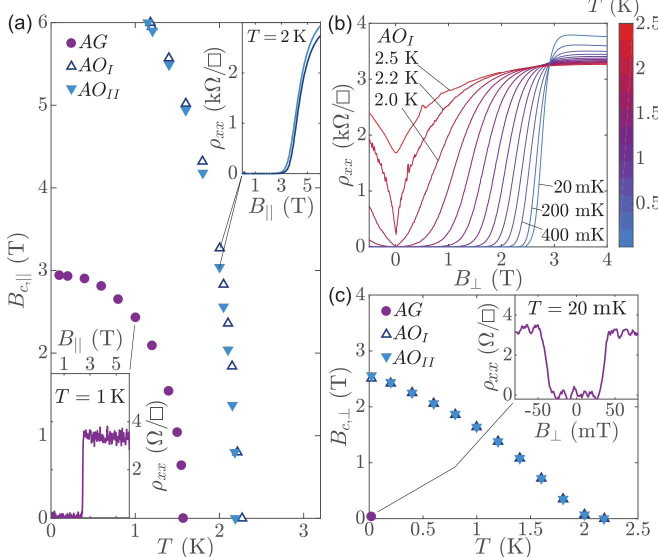

FIG. 3. Transport data from sample 1. (a) Critical in-plane field of as-grown (AG) and anodic-oxidation (AO) Hall bars as a function of temperature, T. Insets: Examples of ρ_{xx} versus $B_{\parallel}$ at elevated temperatures, 1 K and 2 K, used for extracting $B_{c,||}$ points marked by lines. (b) AO_I longitudinal resistance ρ_{xx} as a function of perpendicular field, $B_{\perp}$, at different temperatures. Note field-driven superconductor-insulator transition at $B_{\perp} \sim 3$ T. (c) Same as (a) but for $B_{\perp}$, extracted from data in (b) with $\rho_{xx}(B_{c,\perp}) = 0.01\,\rho_N$. Inset: AG ρ_{xx} versus $B_{\perp}$ at base temperature.

field, $B_{c,||}$, for sample 1 is shown in Fig. 3(a) as a function of temperature, T. The GaAs substrate of sample 1 is insulating at low temperature. Four-terminal longitudinal resistivity, ρ_{xx}, was measured on two devices, AO_I, AO_{II}, both anodized at 4 V, and on a third device with Al as grown (AG) without AO. For the two AO samples we observe $B_{c,||} > 6$ T at base temperature and $B_{c,||} = 6$ T at 1.2 K, while the AG shows $B_{c,||} = 3$ T at base temperature. Figure 3 indicates that the two AO devices were essentially identical. Additional scans are displayed in SM Sec. E [41].

For the AG device, the normal state resistivity is low, $\rho_{N,\mathrm{AG}} = 3.5\ \Omega/\square$, and the transition is sharp, while the AO Hall bars have higher resistivity, $\rho_{N,\mathrm{AO}} \sim 3.5\ \mathrm{k}\Omega/\square$, and a broad transition. The thousandfold increase in normal-state resistivity in the AO film compared to the AG film presumably reflects increased scattering [44] and inhomogeneity, not simply reduced thickness. $B_{c,||}$ was defined as $\rho_{xx}(B_{c,||}) = 0.01\,\rho_N$. Temperature sweeps were also used to extract $T_c(B_{\parallel} = 0)$. AG has $T_c = 1.6$ K while AO_I has $T_c = 2.3$ K.

For a BSC-like superconductor with $T_c = 2.3$ K, the theoretical Chandrasekhar-Clogston (CC) limit [45,46] for the critical field, assuming a metallic Lande g factor of 2, is $B_c(T = 0) \sim 4.6$ T, which is clearly violated in these samples. Violation of CC limit has earlier been reported on a Pb film [47], where the authors claim that the spins are momentum locked in Rashba subbands due to high spin-orbit energy, which suppresses Zeeman splitting. A related suppression of Zeeman splitting could originate from the high surface-to-bulk ratio of the anodized films, which could lead to large Rashba spin-orbit coupling within the film [48].

Critical perpendicular magnetic field as a function of temperature $B_{c,\perp}(T)$, is displayed in Figs. 3(b) and 3(c). We determine $B_{c,\perp}$ as the field for which $\rho_{xx}(B_{c,\perp}) = 0.01\,\rho_N$. A base-temperature scan of the AG sample yielded $B_{c,\perp} = 32$ mT, higher than the bulk Al value $B_c \sim 10$ mT [49]. Scans used to determine $B_{c,\perp}(T)$ for AO_I are shown in Fig. 3(b). Extracted critical fields for AO_I and AO_{II} are shown in Fig. 3(c) (AO_{II} scans are shown in SM Sec. E [41]). A nearly two orders of magnitude increase in $B_{c,\perp} = 2.5$ T is observed. This is comparable with $B_{c,\perp}$ extrapolated from measurements on granular aluminum [34,35].

Just below 3 T, a crossover point for different isotherms is observed. Such crossovers indicate superconductor-insulator transitions, studied in thin and/or disordered superconductors [50–54]. A similar crossing was not observed in the probed range of $B_{\parallel}(T)$, but it might occur beyond 6 T. The resistance jumps seen below 1 T at high temperatures track temperature fluctuations, which were monitored simultaneously.

Comparing $B_{c,||}(T)$ and $B_{c,\perp}(T)$, the latter has a more linear T dependence. This is expected from Ginzburg-Landau theory and previously observed in thin quench-condensed Al films [55]. Another feature worth highlighting is the upward curvature of $B_{c,\perp}$(T) for $T \lesssim T_c$, previously observed in thin granular aluminum [56], where the authors attributed the effect to electron localization and electron-electron interaction.

V. ANODIZED Al on InAs 2DEG: TRANSPORT STUDIES

Transport measurements of sample 2, comprising AO of epitaxial Al on a heterostructure with a shallow InAs 2DEG, show similar trends in field and temperature as Al on insulating GaAs, with the addition of transport signatures from the 2DEG at $B_{\perp} > B_{c,\perp}$. Figure 4(a) shows $B_{c,||}(T)$ for Hall bars from device α and β, anodized at $V_{\mathrm{AO}} = 3.5$ V and 4.2 V respectively, as well as a Hall bar with as-grown aluminum, (AG_2), the subscript indicating sample 2. The data are extracted from $\rho_{xx}(B_{\parallel})$ scans at fixed temperature. Lower-left inset displays $\rho_{xx}(B_{\parallel})$ from AG_2 and 3.5 V Hall bars measured at 20 mK, showing a sharp superconducting transition. Top-right inset presents 4.2 V measurements of $\rho_{xx}(B_{\parallel})$ at 1.8 K, showing broad superconducting transitions. The full set of measurements are included in SM Sec. F [41].

AG_2 has a normal state resistivity $\rho_{N,\mathrm{AG}} = 6\,\Omega/\square$. On both α and β, the Al anodized with 3.5 V has $\rho_{N,3.5,\alpha} = \rho_{N,3.5,\beta} = 61\,\Omega/\square$. The Al anodized with 4.2 V has $\rho_{N,4.2,\alpha} = 120\,\Omega/\square$ and $\rho_{N,4.2,\beta} = 160\,\Omega/\square$ and broad superconducting transitions. Here, the critical fields are again extracted as $\rho_{xx}(B_{||,c}) = 0.01\,\rho_N$. T_c at 0 and 6 T was obtained through temperature sweeps at those fields. The critical field and temperature for AG_2 are $B_{c,||} = 2.5$ T and $T_c = 1.7$ K while for the 3.5 V films, $B_{c,||} = 5.4$ T and $T_c = 2.3$ K. The thinnest films, using 4.2 V AO on α and β, have in-plane critical fields exceeding 6 T. We again attribute surpassing the CC limit to a large Rashba spin-orbit coupling from a high surface-to-bulk ratio. The critical temperature at 0 and 6 T are 2.3 K and 1.3 K for 4.2 V on device α and 2.1 K and 1.0 K for 4.2 V on device β.

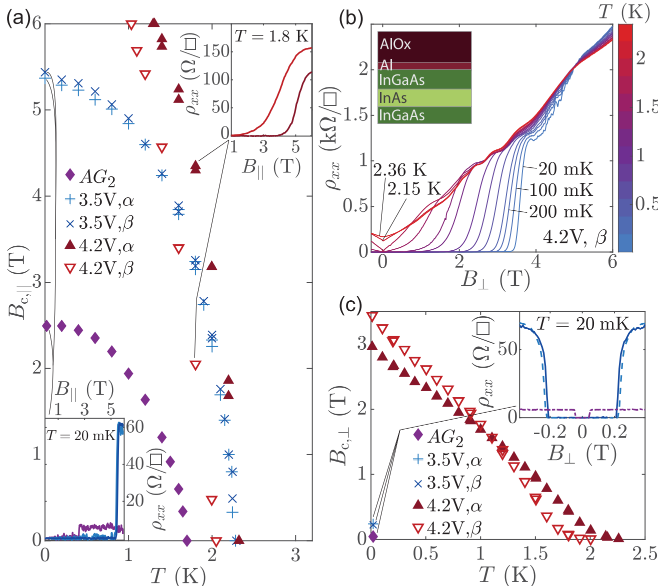

FIG. 4. Transport data from sample 2. (a) Critical in-plane field, $B_{c,||}$, as a function of temperature, T, for as grown Al, AG_2, and $V_{AO} = 3.5$ and 4.2 V Hall bars on devices α and β. Some of the 3.5 and 4.2 V points were measured twice. Examples of $\rho_{xx}(B_{\|})$ scans are included in the insets, taken at the stated temperatures. (b) ρ_{xx} as a function of $B_\perp$ at different temperatures for the anodized Al film at 4.2 V. Inset: Heterostructure of sample 2. (c) Extraction of $B_{c,\perp}(T)$ for both Al films anodized at 4.2 V including base temperature $B_{c,\perp}$ for both Hall bars anodized at 3.5 V and for AG_2, extracted from scans displayed in the inset.

Both of the sample-2 AO Hall bars using $V_{AO} = 4.2$ V have resistivities an order of magnitude lower than the resistivity of AO_I on GaAs, due to parallel conduction through the 2DEG. The fact that $\rho_{N,4.2,\beta} > \rho_{N,4.2,\alpha}$ indicate that the Hall bar β has a thinner or more disordered Al film. It also has a lower T_c indicating that we are beyond the optimal thickness or disorder for T_c after which it is expected to drop [35,57]. The notable difference between the two 4.2-V Hall bars indicates a lack of repeatability. For these few-ML-thick aluminum films a small change in thickness or disorder have a large impact on the transport, making these films good probes for repeatability. The devices were made simultaneously from the same fabrication steps. Discrepancies could arise from sensitivity to the time over which AO was carried out, or due initial nonuniformity in the Al thickness, even in the ML range.

Figure 4(b) shows $\rho_{xx}(B_\perp)$ scans at different temperatures of the $V_{AO} = 4.2$ V, β device, while data from $V_{AO} = 4.2$ V, α is shown in SM Sec. F [41]. In both cases we again see a crossing of the isotherms, but on the GaAs substrate, Fig. 3(b), $\rho_{xx}(B_\perp)$ converges shortly after the crossing. On InAs, at least up to 6 T, $\rho_{xx}(B_\perp)$ keeps changing, possibly due to $B_\perp$-induced orbital effects in the 2DEG, which we investigate in Ref. [58].

Even though the normal state resistances increase in $B_\perp$, to extract $B_{c,\perp}(T)$, we use 1% of the same ρ_N that was used when extracting $B_{c,||}(T)$. The result is displayed on Fig. 4(c) together with extractions from the other four Hall bars. Both of the 3.5 V and the AG_2 Hall bar were only

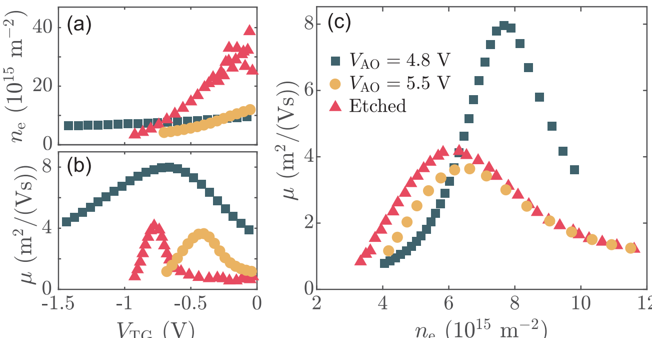

FIG. 5. Dependence of mobility, μ, and electron density, n_e, on top-gate voltage, V_{TG}, for three devices from sample 2, identified by legend in (c). The red triangle is from a device where Al was chemically wet etched. The yellow circles and blue squares are from Hall bars anodized at 5.5 V and 4.8 V, respectively. (a) Density as a function of top-gate voltage. (b) Mobility as a function of top-gate voltage. (c) Parametric plot of mobility as a function of density.

measured at base temperature, line scans shown in the inset. $B_{c,\perp}(T \sim 20 \text{ mK}) = 40$ mT for AG_2 Hall bar, 230 mT for the 3.5 V Hall bars, while 4.2 V, α and β has $B_{c,\perp} = 3.0$ T and 3.5 T, respectively. As observed for anodized Al on GaAs substrate, Fig. 3(c), these films resemble granular Al, with $B_{c,\perp}$ increased by more than two orders of magnitude and with the $B_{c,\perp}(T)$ dependence being close to linear with an upward curvature close to T_c.

VI. PASSIVATION OF SHALLOW InAs 2DEG

Further increase of V_{AO} resulted in Hall bars having finite resistance at base temperature, indicating a full oxidation of the Al film. Such an outcome allows the semiconductor underneath to be passivated and 2DEG density to be controlled with the top-gate. Top gating was found to be possible on Hall bars anodized at $V = 4.8$ V and 5.5 V, see Figs. 5(a) and 5(b), indicating that the residual metallic Al film was either discontinuous or completely oxidized.

Characterization of the two Hall bars was done measuring longitudinal resistivity ρ_{xx} and Hall resistivity $\rho_{xy} = dV_{xy}/dI$ as a function of $B_\perp$ and top-gate voltage, V_{TG}, to extract carrier density, n_e, and carrier mobility, μ, from the low field Hall effect. The same analysis has been performed on a Hall bar fabricated with standard chemical wet etch of the Al film. The V_{TG} dependence of mobility, μ, versus density, n_e for the three Hall bars is shown in Fig. 5. Details concerning the fabrication of the etched Hall bar and additional quantum Hall data of another Hall bar, also anodized at 4.8 V, are given in SM Sec. G [41].

Carrier density as a function of V_{TG} is shown in Fig. 5(a). For all Hall bars, n_e decreased monotonically with negative gate voltage V_{TG} (the etched Hall bar was noisy for $V_{TG} > -0.3$ V). At $V_{TG} = 0$, the etched Hall bar has $n_e \sim 4 \times 10^{16}$ m^{-2}, while the Hall bars anodized at 5.5 V and 4.8 V has $n_e = 1.1 \times 10^{16}$ m^{-2} and $n_e = 9.8 \times 10^{15}$ m^{-2}, respectively. The same order is observed in the slope of n_e versus V_{TG}, with the etched Hall bar having the steepest slope and the 4.8 V Hall bar slope being most flat. Corresponding mobilities are shown in Fig. 5(b) as a function of V_{TG} and in Fig. 5(c) as

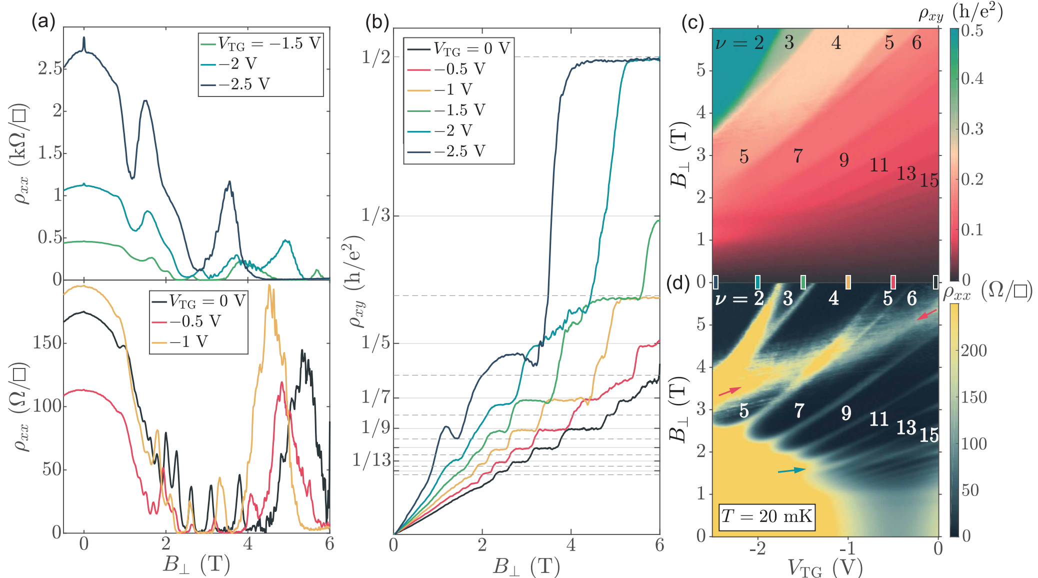

FIG. 6. Quantum Hall regime at base temperature for Hall bar anodized at 4.8 V. (a) Longitudinal and (b) Hall resistivities as a function of $B_\perp$ for different top-gate voltages. In (b) the quantum Hall resistivities for odd (solid) and even (dashed) integer filling factors marked. 2D map of the (c) Hall and (d) longitudinal resistivities as a function of $B_\perp$ and top-gate voltage, V_{TG}. Extracted filling factors are indicated on the maps. Arrows in (d) highlight additional resonances.

function of n_e. We speculate on the origin of the nonmonotonic dependence of mobility with density: At low densities, the initial increase in μ with increasing n_e presumably reflects an increased range of validity for Thomas-Fermi screening. A peak in mobility followed by a decrease with further increase of n_e presumably reflects a greater concentration of electrons at the surface.

The wet-etched Hall bar has a mobility peak of 4.2 $\mathrm{m^2/V\,s}$ at $n_e = 6.1 \times 10^{15}\ \mathrm{m^{-2}}$, which is high for a shallow 2DEG structure, taking into account that this 2DEG has transparent coupling to the Al, as shown in Ref. [23]. The Hall bar anodized at 4.8 V has an increased mobility peak of 8.0 $\mathrm{m^2/V\,s}$ at $n_e = 7.7 \times 10^{15}\ \mathrm{m^{-2}}$ while the 5.5 V AO Hall bar has a reduced mobility peak of 3.7 $\mathrm{m^2/V\,s}$ at $n_e = 6.5 \times 10^{15}\ \mathrm{m^{-2}}$. It is known that the aluminum etch damages the underlying semiconductor [5], partially due to the exposure to atmosphere [32]. We attribute the increased peak mobility after 4.8 V AO to an alumina passivation of the III-V, as depicted in Fig. 1(g), decreasing surface scattering compared to the etched Hall bar. AO at 5.5 V showed decreased peak mobility compared to the etched Hall bar. We suspect that such a voltage introduces disorder by contributing to oxidation of the semiconductor underneath, as depicted in Fig. 1(g).

Measurements of ρ_{xx} and ρ_{xy} as a function of V_{TG} and $B_\perp$ up to 6 T are shown in Fig. 6. These data are for the highest mobility Hall bar, anodized at 4.8 V. Figure 6(a) shows ρ_{xx} as a function of $B_\perp$ for different V_{TG} between 0 and -2.5 V. Exponential increase of the zero-field ρ_{xx} when biasing V_{TG} negatively suggests good gateability through the anodized Al. Shubnikov de Haas oscillations (SdHO) are visible for $B_\perp > 1$ T with vanishing minima of ρ_{xx} for $B_\perp \sim 2.5$ T. We emphasize that this value of field is ~ 1 T *lower* than our highest superconducting $B_{c,\perp}$. Along with vanishing ρ_{xx}, quantized plateaus of ρ_{xy} are observed in Figure 6(b) for ρ_{xy} with $B_\perp > 2$ T, indicating that the sample is within the quantum Hall regime at fields below $B_{c,\perp}$.

Besides SdHO, extra ρ_{xx} peaks are present in Fig. 6(a). Starting at the least negative V_{TG}, a broad and tall resistivity spike is observed between 4 and 6 T and a smaller increment to ρ_{xx} is observed just below 2 T. For the most negative V_{TG}, the high field spike moves towards 3 T, and the increment below 2 T becomes more prominent. Lastly a weak localization peak [59] is observed around $B_\perp = 0$.

Additional features are observed in the Hall resistivity as well. At fields where ρ_{xx} has additional spikes, ρ_{xy} is noisy and forms noninteger plateaus. Below 4 T, ρ_{xy} only has plateaus at odd fractions. This is seen more clearly in Fig. 6(c), displaying a color map of $\rho_{xy}(V_{\mathrm{TG}}, B_\perp)$, from which we extract the filling factor ν and display it across the map. The same ν are added to a color map of $\rho_{xx}(V_{\mathrm{TG}}, B_\perp)$, Fig. 6(d), showing a Landau fan diagram with additional features. The most obvious of these, a resonance crossing the fan at high fields, marked by red arrows, is the origin of the high field resistance spikes mentioned above. We notice that above the resonance, ν has regular even integer counting with spin-splitting into odd values around $B_\perp \sim 5$ T. Below the resonance, ν obtains odd integer counting. Another, less prominent, resonance, marked by the blue arrow, is the origin of the increment and spikes below 2 T in Fig. 6(a). A better visualization of the low-field features is obtained from an un-saturated color map of $\rho_{xx}(V_{\mathrm{TG}}, B_\perp)$ included in SM Sec. H [41].

Similar high field studies, presented in SM Sec. H [41], were done on two other Hall bars; the other bar anodized at 4.8 V and an etched Hall bar. Both studies display similar additional ρ_{xx} resonances. In all cases, the resonances have a weaker V_{TG} dependence than the respective 2DEG Landau fans, suggesting the presence of an additional subband residing in the heterostructure below the InAs 2DEG.

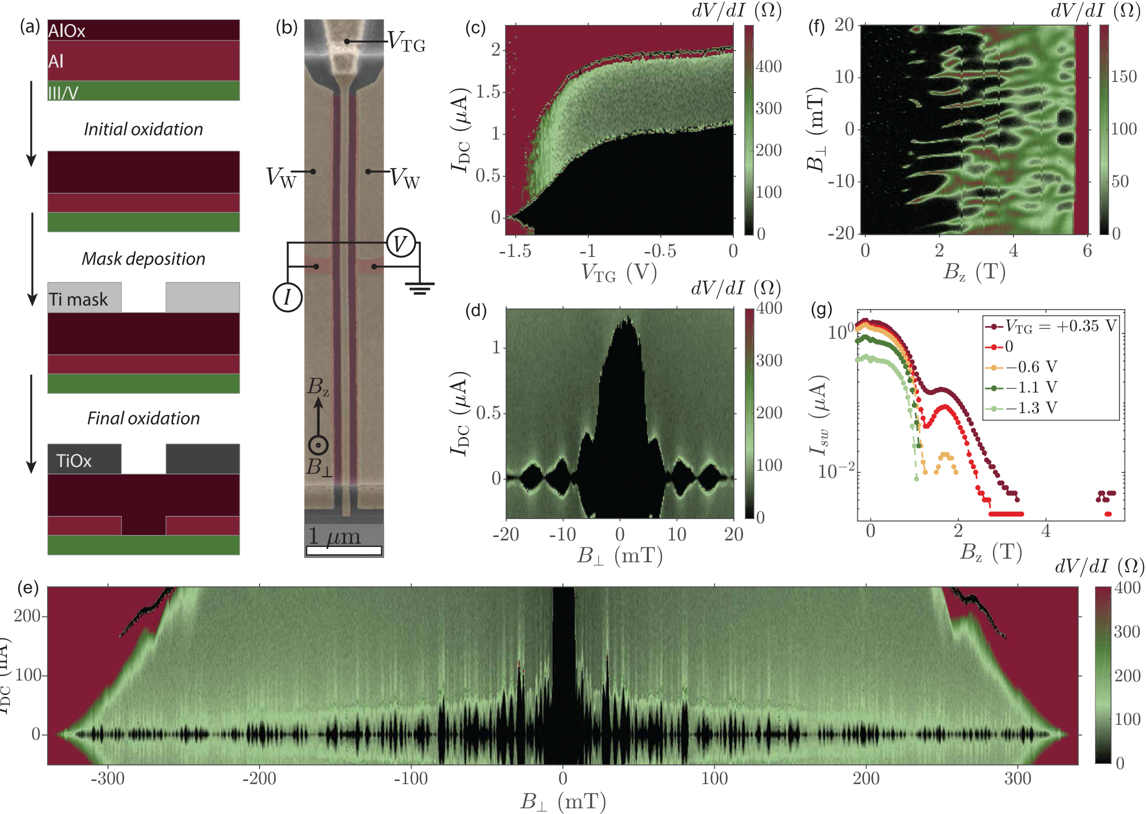

FIG. 7. (a) Schematic illustration of the fabrication process combining standard lithography techniques with metal masks and anodic oxidation. (b) False-color scanning electron micrograph of the reported narrow Josephson junction. The remaining thin Al layer is in red, and the gates are represented in yellow. The two side gates V_W are kept at −1.6 V for the experiments. Transport was current-biased with voltage drop, V, measured in a four-terminal configuration. Field directions $B_\perp$ and B_z are defined in the bottom left part of the figure. (c) Saturated color map of the differential resistance dV/dI as a function of current bias I_{dc} and top-gate voltage V_{TG}. (d) Saturated color map of dV/dI as a function of current bias and perpendicular field for $V_{TG} = 0$. (e) Extended color map of dI/dV as a function of I_{dc} and $B_\perp$ showing supercurrent oscillations surviving high fields $B_\perp > 300$ mT, with $V_{TG} = 350$ mV. (f) Saturated color map of dV/dI at zero bias as a function of $B_\perp$ and B_z, showing that the supercurrent is oscillating as a function of both field directions, with $V_{TG} = 0$. (g) Oscillation and re-emergence of switching current, I_{sw} (see main text) vs. B_z for several top-gate voltages, V_{TG}.

Speculations about the rise of extra resonances in ρ_{xx} and the addition to ν that comes with them, lead to an interpretation including a low density and disordered second band. The extra resonances represent its fan diagram. The broad fans indicate low mobility. To explain the observed combined filling factor ν, we suggest that crossing the high field resonance, marked by red arrows in Fig. 6(d), takes the second band filling factor from $\nu_{2nd} = 1$ to 0. Depletion of a Hall bar with $B_\perp$ is commonly observed in the study of disordered 2DEGs [60]. The origin of such a second band and where it would reside is not clear. It could be related to an unintentional quantum well deeper in the heterostructure.

VII. PATTERNING ANODIC OXIDATION

Combining lithography with anodic oxidation opens a new path toward patterning hybrid heterostructures. In this section, we demonstrated patterning of the AO process, implemented on the InAs 2DEG heterostructure, sample 2. Following a few unsuccessful approaches to patterning, described in SM Sec. I [41], a successful metal-mask approach was implemented, as shown in Fig. 7(a). Following an initial global AO step, a thin Ti metal mask was patterned using electron beam lithography and liftoff, with Ti in the locations where Al should stay metallic. A second AO fully oxidizes the Al not covered by the mask as well as oxidizing the mask itself. Resulting structures are shown in SM Sec. J [41].

The initial oxidation was done at 3.5 V for 5 min. The resulting Al film had $B_{c,||} \approx 5.6$ T and $B_{c,\perp} \approx 300$ mT, similarly to the 3.5 V exposures of Fig. 4, indicating a similar thickness.

A final oxidation was done at 4.8 V for 5 min. The Hall bar showed a mobility peak of 1.16 m^2/V s at a density of 7.2×10^{15} m^{-2}. The mobility is much lower than the one reported for Hall bars in Fig. 5, suggesting the oxidation process was too deep and impacted the semiconductor.

An unintended oxidation depth could be due to a time-dependent AO process, see SM Sec. A [41]. The final oxidation, having the largest V_{AO}, was intended to solely control the oxidation thickness. With a time-dependence, the depth of the initial and final oxidation would add up, making our current setup nonideal for this purpose.

This method was used to fabricate 5-μm-long superconductor-normal-superconductor Josephson junction (JJ) with 100 nm wide superconducting leads and normal

regions varied between 100 and 400 nm, as shown in see Fig. 7(b) and SM Sec. K [41].

Measurement setup and applied field directions are also shown in Fig. 7(b). An out-of-plane field $B_\perp$ is used in combination with an in-plane field B_z, perpendicular to the junction. An ac current bias of 0.5 nA was applied with possibility of adding dc bias, $I_{\rm dc}$, while an ac voltage drop was measured. A top-gate $V_{\rm TG}$ was used to deplete or populate the junction with carriers. The two wire gates V_W, biased at $= -1.6$ V, were used to form the narrow junction in the InAs 2DEG enabled by electrostatic screening of the metallic aluminum [23].

Gate control of the supercurrent is shown in Fig. 7(c). Differential resistance (dV/dI) is measured as a function of $I_{\rm dc}$ and $V_{\rm TG}$, which related a critical current $I_c \sim 1.1$ μA at $V_{\rm TG} = 0$ V. The Fraunhofer-like pattern of oscillations of critical current as function of perpendicular magnetic field, $B_\perp$ is shown in Fig. 7(d). We observe that the critical current oscillates in $B_\perp$ as seen previously [23,61–63]. For an ideal junction, the critical current is expected to follow:

$$I_c(B_\perp) = I_c(0)\left|\frac{\sin(\pi B_\perp A/\phi_0)}{\pi B_\perp A/\phi_0}\right|, \qquad (1)$$

ϕ_0 being the flux quantum and A being the junction area which, in our case, is designed to be $\sim$0.1 μm $\times$ 5 μm = 0.50 μm^2. The observed period of $\sim$4.5 mT corresponds to an area of 0.46 μm^2, not far from the designed value.

The perpendicular critical field is estimated to be 310 mT as evidenced in the large field Fraunhofer pattern of Fig. 7(e). This value is consistent with the critical field of full-sheet anodized Al, see SM sec. J [41].

The narrow JJs were made to verify the resolution of the AO lithography with metal masks. A gateable junction verifies that the Al leads are not shorted and the Fraunhofer period indicates that the leads are not broken. This indicates that the horizontal lithographic resolution is better than 50 nm, both away from and in-under the metal mask.

Differential resistance dV/dI was measured at $I_{\rm dc} = 0$ as a function of B_z and $B_\perp$ with $V_{\rm TG} = 0$, displayed on Fig. 7(f). Similar maps were taken at other $V_{\rm TG}$ values, see SM Sec. L [41]. The field directions were aligned to the device axes before data acquisition. A complicated pattern is observed with quenching and reappearance of the supercurrent as a function of both field directions. For $B_z < 1$ T, supercurrent persists for all $B_\perp \in [-20 : 20]$ mT. Beyond 1 T resistive regimes emerges and broadens out. No supercurrent is present after $B_z > 4$ T, besides two superconducting blobs appearing at high fields $B_z \sim 5.5$ T, just before the Al goes normal.

Switching current, $I_{\rm sw}$, defined as the maximum critical current for any $B_\perp$ in a 10 mT interval, as a function of B_z between -0.3 T and 5.8 T for $V_{\rm TG}$ between $+0.3$ V and -1.3 V is shown in Fig. 7(g). For $V_{\rm TG} = -1.3$ V and -1.1 V, we observe the supercurrent being quenched around $B_z \sim 1$ T. For $V_{\rm TG} = -0.6$ V, the junction goes resistive as well around $B_z \sim 1$ T, but superconductivity reemerges between 1.5 and 2 T. For $V_{\rm TG} = 0$ and $+0.35$ V, $I_{\rm sw}$ sustains up to $\sim$3.4 T, with a local peak around 1.7 T. A finite $I_{\rm sw}$ was also observed for B_z between 5.2 and 5.5 T, close to the critical field of the superconductor itself. Resistance of the junction in the normal regime also oscillates with B_z but out of phase with the $I_{\rm sw}$ oscillations, as can be seen in SM Sec. L [41]. We observe that the B_z values for peaks and dips in $I_{\rm sw}$ are independent of $V_{\rm TG}$ and thus also the InAs chemical potential. The B_z value resulting in a topological phase transition is expected to have a chemical potential dependence [21,22]. We therefor attribute the oscillations to be B_z-induced orbital effects as reported in Ref. [23]. For an orbital effect, periodic nodes and antinodes should be expected. With $I_{\rm sw}$ peaks at $B_z \sim 1.7$ T and $\sim$5.4 T, we could be observing 1st and 3rd antinode, while a second antinode around $B_z \sim 3.5$ T could be suppressed.

VIII. CONCLUSION

In summary, we have developed an anodic oxidation approach to controlling the thickness of epitaxially grown Al on hybrid Al-InAs heterostructures. We apply this process to (i) thin epitaxially grown Al resulting in increased critical temperature and magnetic fields, (ii) passivate hybrid heterostructures with complete oxidation of the Al films so that the interface between the heterostructure and oxide has never been exposed to air, and (iii) pattern superconductor-normal junctions when combined with lithographic processes to produce nanoscale structured superconducting elements, focusing on the case of SNS junctions with sub-100 nm features.

The anodized Al films showed critical fields $B_{c,||} > 6$ T and $B_{c,\perp} \sim 3.5$ T. Resistivity of thin disordered Al yielded $\rho_{xx} > 1$ kΩ, making the material interesting for high-kinetic impedance superconducting resonators [64].

Full oxidation of the Al increases peak mobility to 8 m^2/V s, twice the value obtained with regular Al etch. Quantum Hall effect was observed at $\sim$2.5 T, giving $\sim$1 T overlap with highest superconducting critical field, enabling future research into superconductor-quantum Hall hybrids. Applying a metal mask, lithographic resolution <50 nm was achieved.

The different possibilities offered by the anodic oxidation process combined with the improved properties of the resulting films motivate further research in anodic oxidation or other new fabrication processes for hybrid heterostructures. This opens the path towards new applications and new regimes for experiments on hybrid heterostructures.

ACKNOWLEDGMENTS

The authors acknowledge Abhishek Banerjee, Mikhail Feigel'man, Joshua Folk, Roman Lutchyn, and Christoph Strunk for valuable discussions and Saeed Fallahi, Tailung Wu, and Teng Zhang for assistance with measurements. This work was supported by Microsoft Corporation, the Danish National Research Foundation, and the Villum Foundation. Fabrizio Nichele acknowledges support from European Research Commission, Grant No. 804273. STEM studies and all related sample preparation were done at the Birck Nanotechnology Center, Purdue University.

[1] P. Krogstrup, N. L. Ziino, W. Chang, S. M. Albrecht, M. H. Madsen, E. Johnson, J. Nygård, C. M. Marcus, and T. S. Jespersen, Nat. Mater. **14**, 400 (2015).

[2] W. Chang, S. M. Albrecht, T. S. Jespersen, F. Kuemmeth, P. Krogstrup, J. Nygård, and C. M. Marcus, Nat. Nanotechnol. **10**, 232 (2015).

[3] Z. Wan, A. Kazakov, M. J. Manfra, L. N. Pfeiffer, K. W. West, and L. P. Rokhinson, Nat. Commun. **6**, 7426 (2015).

[4] F. Amet, C. T. Ke, I. V. Borzenets, J. Wang, K. Watanabe, T. Taniguchi, R. S. Deacon, M. Yamamoto, Y. Bomze, S. Tarucha, and G. Finkelstein, Science **352**, 966 (2016).

[5] J. Shabani, M. Kjaergaard, H. J. Suominen, Y. Kim, F. Nichele, K. Pakrouski, T. Stankevic, R. M. Lutchyn, P. Krogstrup, R. Feidenhansl, S. Kraemer, C. Nayak, M. Troyer, C. M. Marcus, and C. J. Palmstrøm, Phys. Rev. B **93**, 155402 (2016).

[6] M. Kjaergaard, F. Nichele, H. J. Suominen, M. P. Nowak, M. Wimmer, A. R. Akhmerov, J. A. Folk, K. Flensberg, J. Shabani, C. J. Palmstrøm, and C. M. Marcus, Nat. Commun. **7**, 12841 (2016).

[7] G.-H. Lee, K.-F. Huang, D. K. Efetov, D. S. Wei, S. Hart, T. Taniguchi, K. Watanabe, A. Yacoby, and P. Kim, Nat. Phys. **13**, 693 (2017).

[8] Q. L. He, L. Pan, A. L. Stern, E. C. Burks, X. Che, G. Yin, J. Wang, B. Lian, Q. Zhou, E. S. Choi, K. Murata, X. Kou, Z. Chen, T. Nie, Q. Shao, Y. Fan, S.-C. Zhang, K. Liu, J. Xia, and K. L. Wang, Science **357**, 294 (2017).

[9] F. Krizek, J. E. Sestoft, P. Aseev, S. Marti-Sanchez, S. Vaitiekenas, L. Casparis, S. A. Khan, Y. Liu, T. Stankevič, A. M. Whiticar, A. Fursina, F. Boekhout, R. Koops, E. Uccelli, L. P. Kouwenhoven, C. M. Marcus, J. Arbiol, and P. Krogstrup, Phys. Rev. Mater. **2**, 093401 (2018).

[10] S. Vaitiekenas, A. M. Whiticar, M. T. Deng, F. Krizek, J. E. Sestoft, C. J. Palmstrøm, S. Marti-Sanchez, J. Arbiol, P. Krogstrup, L. Casparis, and C. M. Marcus, Phys. Rev. Lett. **121**, 147701 (2018).

[11] S. Guiducci, M. Carrega, G. Biasiol, L. Sorba, F. Beltram, and S. Heun, Phys. Status Solidi Rapid Res. Lett. **13**, 1800222 (2019).

[12] M. Pendharkar, B. Zhang, H. Wu, A. Zarassi, P. Zhang, C. P. Dempsey, J. S. Lee, S. D. Harrington, G. Badawy, S. Gazibegovic, J. Jung, A. H. Chen, M. A. Verheijen, M. Hocevar, E. P. A. M. Bakkers, C. J. Palmstrøm, and S. M. Frolov, arXiv:1912.06071.

[13] D. J. Carrad, M. Bjergfelt, T. Kanne, M. Aagesen, F. Krizek, E. M. Fiordaliso, E. Johnson, J. Nygård, and T. S. Jespersen, Adv. Mater. **32**, 1908411 (2020).

[14] T. Kanne, M. Marnauza, D. Olsteins, D. J. Carrad, J. E. Sestoft, J. de Bruijckere, L. Zeng, E. Johnson, E. Olsson, K. Grove-Rasmussen, and J. Nygård, arXiv:2002.11641.

[15] R. M. Lutchyn, J. D. Sau, and S. Das Sarma, Phys. Rev. Lett. **105**, 077001 (2010).

[16] Y. Oreg, G. Refael, and F. von Oppen, Phys. Rev. Lett. **105**, 177002 (2010).

[17] T. Karzig, C. Knapp, R. M. Lutchyn, P. Bonderson, M. B. Hastings, C. Nayak, J. Alicea, K. Flensberg, S. Plugge, Y. Oreg, C. M. Marcus, and M. H. Freedman, Phys. Rev. B **95**, 235305 (2017).

[18] F. Nichele, A. C. C. Drachmann, A. M. Whiticar, E. C. T. O'Farrell, H. J. Suominen, A. Fornieri, T. Wang, G. C. Gardner, C. Thomas, A. T. Hatke, P. Krogstrup, M. J. Manfra, K. Flensberg, and C. M. Marcus, Phys. Rev. Lett. **119**, 136803 (2017).

[19] E. C. T. O'Farrell, A. C. C. Drachmann, M. Hell, A. Fornieri, A. M. Whiticar, E. B. Hansen, S. Gronin, G. C. Gardner, C. Thomas, M. J. Manfra, K. Flensberg, C. M. Marcus, and F. Nichele, Phys. Rev. Lett. **121**, 256803 (2018).

[20] A. M. Whiticar, A. Fornieri, E. C. T. O. Farrell, A. C. C. Drachmann, T. Wang, C. Thomas, S. Gronin, R. Kallaher, G. C. Gardner, M. J. Manfra, C. M. Marcus, and F. Nichele, Nat. Commun. **11**, 3212 (2020).

[21] M. Hell, M. Leijnse, and K. Flensberg, Phys. Rev. Lett. **118**, 107701 (2017).

[22] F. Pientka, A. Keselman, E. Berg, A. Yacoby, A. Stern, and B. I. Halperin, Phys. Rev. X **7**, 021032 (2017).

[23] A. Fornieri, A. M. Whiticar, F. Setiawan, E. Portolés, A. C. C. Drachmann, A. Keselman, S. Gronin, C. Thomas, T. Wang, R. Kallaher, G. C. Gardner, E. Berg, M. J. Manfra, A. Stern, C. M. Marcus, and F. Nichele, Nature **569**, 89 (2019).

[24] X. L. Qi, T. L. Hughes, and S. C. Zhang, Phys. Rev. B **82**, 184516 (2010).

[25] R. S. K. Mong, D. J. Clarke, J. Alicea, N. H. Lindner, P. Fendley, C. Nayak, Y. Oreg, A. Stern, E. Berg, K. Shtengel, and M. P. A. Fisher, Phys. Rev. X **4**, 011036 (2014).

[26] M. Cheng, R. M. Lutchyn, and S. Das Sarma, Phys. Rev. B **85**, 165124 (2012).

[27] D. Rainis and D. Loss, Phys. Rev. B **85**, 174533 (2012).

[28] G. E. Blonder, M. Tinkham, and T. M. Klapwijk, Phys. Rev. B **25**, 4515 (1982).

[29] C. W. J. Beenakker, Phys. Rev. B **46**, 12841 (1992).

[30] M. Kjaergaard, H. J. Suominen, M. P. Nowak, A. R. Akhmerov, J. Shabani, C. J. Palmstrøm, F. Nichele, and C. M. Marcus, Phys. Rev. Appl. **7**, 034029 (2017).

[31] A. T. Hatke, T. Wang, C. Thomas, G. C. Gardner, and M. J. Manfra, Appl. Phys. Lett. **111**, 142106 (2017).

[32] S. J. Pauka, J. D. S. Witt, C. N. Allen, B. Harlech-Jones, A. Jouan, G. C. Gardner, S. Gronin, T. Wang, C. Thomas, M. J. Manfra, D. J. Reilly, and M. C. Cassidy, J. Appl. Phys. **128**, 114301 (2020).

[33] P. M. Tedrow and R. Meservey, Phys. Rev. B **25**, 171 (1982).

[34] T. Chui, P. Lindenfeld, W. L. McLean, and K. Mui, Phys. Rev. B **24**, 6728 (1981).

[35] R. W. Cohen and B. Abeles, Phys. Rev. **168**, 444 (1968).

[36] G. Deutscher and S. A. Dodds, Phys. Rev. B **16**, 3936 (1977).

[37] J. W. Diggle, T. C. Downie, and C. W. Goulding, Chem. Rev. **69**, 365 (1969).

[38] V. F. Henley, *Anodic Oxidation of Aluminum and Its Alloys* (Pergamon Press, London, 1982).

[39] S. W. Hieke, B. Breitbach, G. Dehm, and C. Scheu, Acta Mater. **133**, 356 (2017).

[40] Y. Nakamura, D. L. Klein, and J. S. Tsai, Appl. Phys. Lett. **68**, 275 (1996).

[41] See supplemental material at http://link.aps.org/supplemental/10.1103/PhysRevMaterials.5.013805 for complimentary figures and experimental details.

[42] C. C. Ahn (Ed.), *Transmission Electron Energy Loss Spectrometry in Materials Science and EELS Atlas*, 2nd ed. (Wiley, Weinheim, Germany, 2004).

[43] D. Qian, B. Xu, M. Chi, and Y. S. Meng, Phys. Chem. Chem. Phys. **16**, 14665 (2014).
[44] P. Wissmann and H.-U. Finzel, *Electrical Resistivity of Thin Metal Films* (Springer, Berlin, 2007).
[45] B. S. Chandrasekhar, Appl. Phys. Lett. **1**, 7 (1962).
[46] A. M. Clogston, Phys. Rev. Lett. **9**, 266 (1962).
[47] H. Nam, H. Chen, T. Liu, J. Kim, C. Zhang, J. Yong, T. R. Lemberger, P. A. Kratz, J. R. Kirtley, K. Moler, P. W. Adams, A. H. MacDonald, and C.-K. Shih, Proc. Natl. Acad. Sci. USA **113**, 10513 (2016).
[48] O. Dimitrova and M. V. Feigel'man, Phys. Rev. B **76**, 014522 (2007).
[49] C. Ihn, *Introduction to Solid State Physics*, 8th ed. (John Wiley & Sons, New York, 2005).
[50] Y. Ando, G. S. Boebinger, A. Passner, T. Kimura, and K. Kishio, Phys. Rev. Lett. **75**, 4662 (1995).
[51] V. F. Gantmakher, M. V. Golubkov, V. T. Dolgopolov, A. Shashkin, and G. E. Tsydynzhapov, J. Exp. Theor. Phys. Lett. **71**, 473 (2000).
[52] K. Makise, T. Kawaguti, and B. Shinozaki, J. Phys. Conf. Ser. **150**, 052149 (2009).
[53] Y. Xing, H.-L. Fu, H. Liu, Y. Sun, F. Wang, X. Lin, J. Wang, H.-M. Zhang, J.-P. Peng, X.-C. Ma, and Q.-K. Xue, Science **350**, 542 (2015).
[54] C. G. L. Bøttcher, F. Nichele, M. Kjaergaard, H. J. Suominen, J. Shabani, C. J. Palmstrøm, and C. M. Marcus, Nat. Phys. **14**, 1138 (2018).
[55] A. D. C. Grassie, D. B. Green, and A. Benyon, Physica **55**, 243 (1971).
[56] B. Shinozaki, T. Kawaguti, and Y. Fujimori, J. Phys. Soc. Jpn. **52**, 2297 (1983).
[57] Y. Ivry, C. S. Kim, A. E. Dane, D. De Fazio, A. N. McCaughan, K. A. Sunter, Q. Zhao, and K. K. Berggren, Phys. Rev. B **90**, 214515 (2014).
[58] A. C. C. Drachmann, A. Banerjee, A. Fornieri, A. M. Whiticar, C. Thomas, S. Gronin, T. Wang, G. C. Gardner, M. J. Manfra, and C. M. Marcus (unpublished).
[59] B. L. Altshuler, D. Khmel'nitzkii, A. I. Larkin, and P. A. Lee, Phys. Rev. B **22**, 5142 (1980).
[60] I. Glozman, C. E. Johnson, and H. W. Jiang, Phys. Rev. Lett. **74**, 594 (1995).
[61] H. J. Suominen, J. Danon, M. Kjaergaard, K. Flensberg, J. Shabani, C. J. Palmstrøm, F. Nichele, and C. M. Marcus, Phys. Rev. B **95**, 035307 (2017).
[62] A. C. C. Drachmann, H. J. Suominen, M. Kjaergaard, B. Shojaei, C. J. Palmstrøm, C. M. Marcus, and F. Nichele, Nano Lett. **17**, 1200 (2017).
[63] M. C. Dartiailh, W. Mayer, J. Yuan, K. S. Wickramasinghe, A. Matos-Abiague, I. Žutić, and J. Shabani, Phys. Rev. Lett. **126**, 036802 (2021).
[64] N. Maleeva, L. Grünhaupt, T. Klein, F. Levy-Bertrand, O. Dupre, M. Calvo, F. Valenti, P. Winkel, F. Friedrich, W. Wernsdorfer, A. V. Ustinov, H. Rotzinger, A. Monfardini, M. V. Fistul, and I. M. Pop, Nat. Commun. **9**, 3889 (2018).